minerals

MDPI

Article

Geochronological, Geochemical and Sr-Nd-Pb-Hf Isotopic Constraints on the Petrogenesis of Pyroxene Diorites in the Sanchahe Iron-Gold Deposit, Western Shandong

Ming Ma [1,2], Chao Zhang [3], Yadong Li [1,2], Mingbo Gao [2,4], Jilei Gao [1,2,*], Siyuan Li [5], Qiwei Feng [1,2], Jian Li [1], Cui Tao [6] and Yankui Liu [1]

1 No. 1 Institute of Geology and Mineral Resources of Shandong Province, Jinan 250100, China; sddkmaming@163.com (M.M.); lydludi@sina.com (Y.L.); fqw0000002022@163.com (Q.F.); aoxiang198721@163.com (J.L.); yimulin@126.com (Y.L.)
2 Shandong Engineering Laboratory for High-Grade Iron Ore Exploration and Exploitation, Jinan 250100, China; jngmb@126.com
3 School of Resources and Environmental Engineering, Shandong University of Technology, Zibo 255049, China; czhang@sdut.edu.cn
4 Shandong Provincial Bureau of Geology & Mineral Resources, Jinan 250000, China
5 School of Earth Resources, China University of Geosciences, Wuhan 430074, China; siyuanli@cug.edu.cn
6 School of Earth Resources, China University of Geosciences, Beijing 100083, China; cuitao95@163.com
* Correspondence: gjljn@163.com

Abstract: The Sanchahe iron-gold deposit in western Shandong province is located in the southeast of the North China Craton. The skarn type of iron-gold deposit (without copper) is located in the contact belt between pyroxene diorites and Ordovician limestone xenoliths. The zircon U-Pb age of pyroxene diorites is 138.4 ± 1.2 Ma belonging to the Early Cretaceous. Pyroxene diorites (Rittmann index σ = 2.2~2.5) belong to the calc-alkaline series and the SiO_2 content is 55~59%. Furthermore, pyroxene diorites are characterized by high Mg and Na contents and high contents of Sc, Cr, Co, and Ni, indicating that it has a geochemical affinity with mantle-derived magma. All of the samples are enriched in light rare earth elements (LREEs) and depleted in heavy rare earth elements (HREEs), with a weak Eu-negative anomaly. They are also enriched in Cs, Ba and Sr and depleted in high field strength elements (HFSEs) (Nb, Ta, Zr), indicating the involvement of some crustal materials. The whole-rock $(^{87}Sr/^{86}Sr)_I$ values are 0.70824~0.70891, and the $\varepsilon_{Nd}(t)$ values are from −8.1 to −12.5. Two-stage model ages of T_{DM2} are 1591~1928 Ma. The εHf(t) values range from −7.0 to −17.4, and the two-stage model ages of T_{DM2} range from 1629 to 2297 Ma, indicating that the magma was derived from Mesoproterozoic to Neoarchean crusts. Combined with Pb isotopic characteristics, pyroxene diorites may be generated by the partial melting of the enriched lithospheric mantle, which had been metasomatized by the ancient lower crust materials of the North China Craton and formed in the strong extensional tectonic setting linked with lithospheric thinning, which may be caused by the rollback of the Pacific plate after subduction.

Keywords: iron-gold deposit; geochronology; geochemical; Sr-Nd-Pb-Hf isotopic; Sanchahe area; West Shandong

Citation: Ma, M.; Zhang, C.; Li, Y.; Gao, M.; Gao, J.; Li, S.; Feng, Q.; Li, J.; Tao, C.; Liu, Y. Geochronological, Geochemical and Sr-Nd-Pb-Hf Isotopic Constraints on the Petrogenesis of Pyroxene Diorites in the Sanchahe Iron-Gold Deposit, Western Shandong. *Minerals* **2022**, *12*, 601. https://doi.org/10.3390/min12050601

Academic Editor: William L. Griffin

Received: 24 March 2022
Accepted: 6 May 2022
Published: 10 May 2022

1. Introduction

Many large gold deposits have been discovered in the Jiaodong area, which is the most important gold metallogeny area in China [1]. The Yishu fault is a boundary fault between the western Shandong province and the Jiaodong area. Considering the similar tectonic setting and contemporary magmatic events between the western Shandong province and the Jiaodong area, although the number and scale of gold deposits are far less than those of the gold deposits in the Jiaodong area, the western Shandong province has the potential for the exploration of gold deposits. After the discovery of the Guilaizhuang gold deposit

in the early 1990s, there has been no breakthrough in gold exploration in the western Shandong province. Thus, the discovery of a Sanchahe Fe-Au skarn deposit is valuable for studying the genesis of skarn Fe-Au deposit and could supply the theoretical basis for exploring the Fe-Auskarn deposit.

Since the 1980s, great progress has been made in exploring and studying the Au skarn deposits. The Au skarn deposits contribute to more than 1000 tons of the gold resources in the world [2]. In China, Au resources from skarn deposits make up about 700 tons, accounting for about 15% of total gold resources. Generally, Au skarn deposits are associated with copper, but Fe-Au skarn deposits are rarely reported in the world. Previous studies have shown that the skarn deposits formed near or in the contact zone between intermediate-acidic plutons and carbonates, and have experienced the metasomatism between hydrothermal fluids and surrounding rocks [3]. Furthermore, the mineralization has a close relationship with the magmatic rocks. Thus, it is significant for studying the ore deposit genesis and exploring the ore deposits to discuss the petrogenesis and the magma source of magmatic rocks. Based on different aspects of the studies on the Early Cretaceous plutons located in the western Shandong province, it has been determined that the source of magma is from the partial melting of the upper mantle which was mixed with the crustal materials. Nevertheless, the source of crustal materials is still up for debate. Different opinions are described as follows: (1) the delaminated lower crust of the North China Craton [4–6], (2) the crustal materials of the Yangtze Craton [7], and (3) the oceanic crustal materials of the Paleo-Pacific [8,9].

The Sanchahe iron-gold deposit is located in the southeast of the North China Craton and is the skarn type iron-gold deposit (without copper) in western Shandong province. The orebody is located in the contact zone between pyroxene diorites and Ordovician limestone. However, the emplacement age and source of pyroxene diorites associated with Sanchahe Fe-Au deposits remain poorly constrained. This study presents zircon U-Pb geochronology, whole rock geochemistry, and Sr-Nd-Pb-Hf isotopic compositions to discuss the emplacement age and petrogenesis of pyroxene diorites.

2. Geological Background and Deposit Characteristics

2.1. Regional Geology

The western Shandong province in the southeastern North China Craton is to the northwest of the Sulu ultrahigh-pressure (UHP) metamorphic belt and is located at the Lankao–Liaocheng fault to the west, the Qihe–Guangrao fault to the north, the Tanlu fault to the east, and the Fengpei fault to the south [5,10] (Figure 1). The study area in this paper is in the middle of western Shandong province and to the northwest of the Taiwu depression. The crystalline basement in the study area is Neoarchean granitoids of the Taishan groups, whereas the sedimentary cover includes Cambrian–Ordovician limestone, Mesozoic clastic rock, and Cenozoic sediments. The faults in the study area are mainly in the direction of NNW, NE, and EW. Furthermore, the NNW trending fault is the main fault in the region. As an important NNW fault, the Tongyedian–Sunzu fault is about 130km long and is the space and channel of the magma. It is characterized by the multi-stage movements of faults, so the magmatic activities including Neoarchean granitoids and Yanshanian granitic complexes have a close relationship with the Tongyedian–Sunzu fault. As part of Yanshannian magmatic activities, Tietonggou granitic complexes with 7.5 km^2 of exposed area are near the Tietonggou area in the southeast of Laiwu and are at the junction of the Tongyedian–Sunzu fault and Qingnigou fault (Figure 2). According to the field geological investigation, Tietonggou granitic complexes are composed of monzogranites, quartz diorite porphyrite, hornblende porphyrite, pyroxene diorite, hornblende, and olivine norite gabbro.

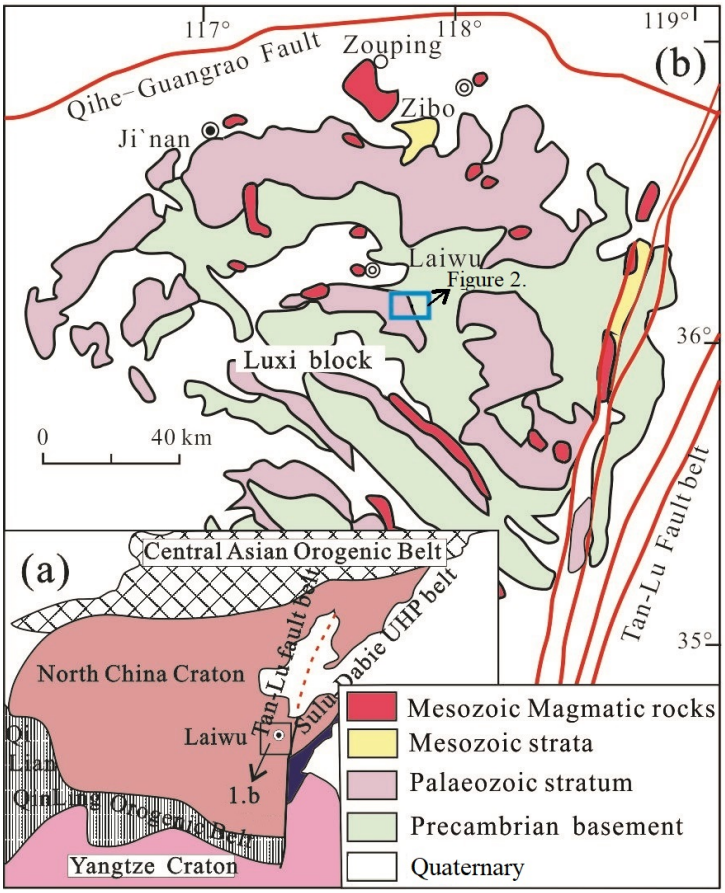

Figure 1. Geological map of the North China Craton (**a**) and geological map of the Luxi terrane (**b**), ((**a**) modified after [11], (**b**) modified after [12]).

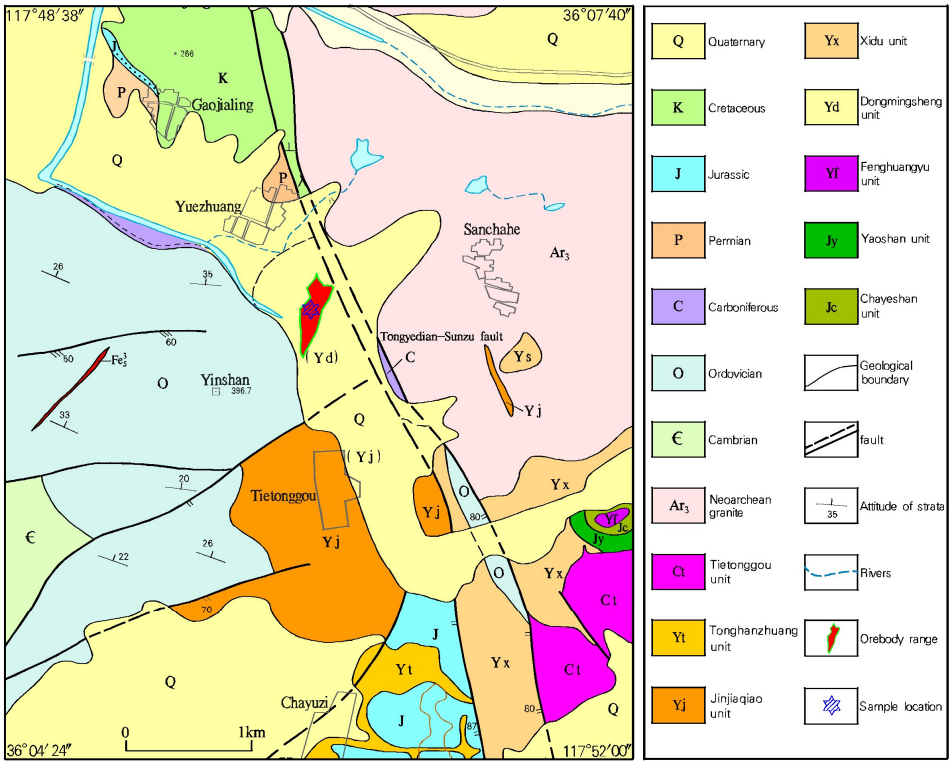

Figure 2. Geological map of the Sanchahe mining area.

2.2. Deposit Characteristics

The Sanchahe deposit is in the north of the Tietonggou granitic complexes, and the ore deposit is under the Quaternary (Figure 2). The pyroxene diorites have a close relationship with the mineralization, and there is skarn metasomatism between the pyroxene diorites and marble. The Fe-Au skarn deposit is composed of Au, Fe, Ag, and S. The orebody is located near the contact zone between magmatic rocks and stratum, whereas the mineralization are mainly distributed in the skarn. The shape of the orebody is stably layered or lenticular, while the local shape of the orebody is consistent with the edge shape of xenoliths. Furthermore, the gold orebody-wrapped iron orebody is thick in the middle and annihilated to both sides (Figure 3). The orebody inclines to the east with an average dip angle of 33°. The average thickness of the gold orebody with an average grade of 4.54 ppm is about 4.65 m, whereas the average thickness of the iron orebody is 2.81 m. The ore types are composed of magnetically mineralized skarn and pyritized magnetically mineralized skarn. The ore minerals include magnetite, pyrite, and gold, whereas the gangue minerals are mainly diopside, tremolite, serpentine, biotite, etc. (Figure 4).

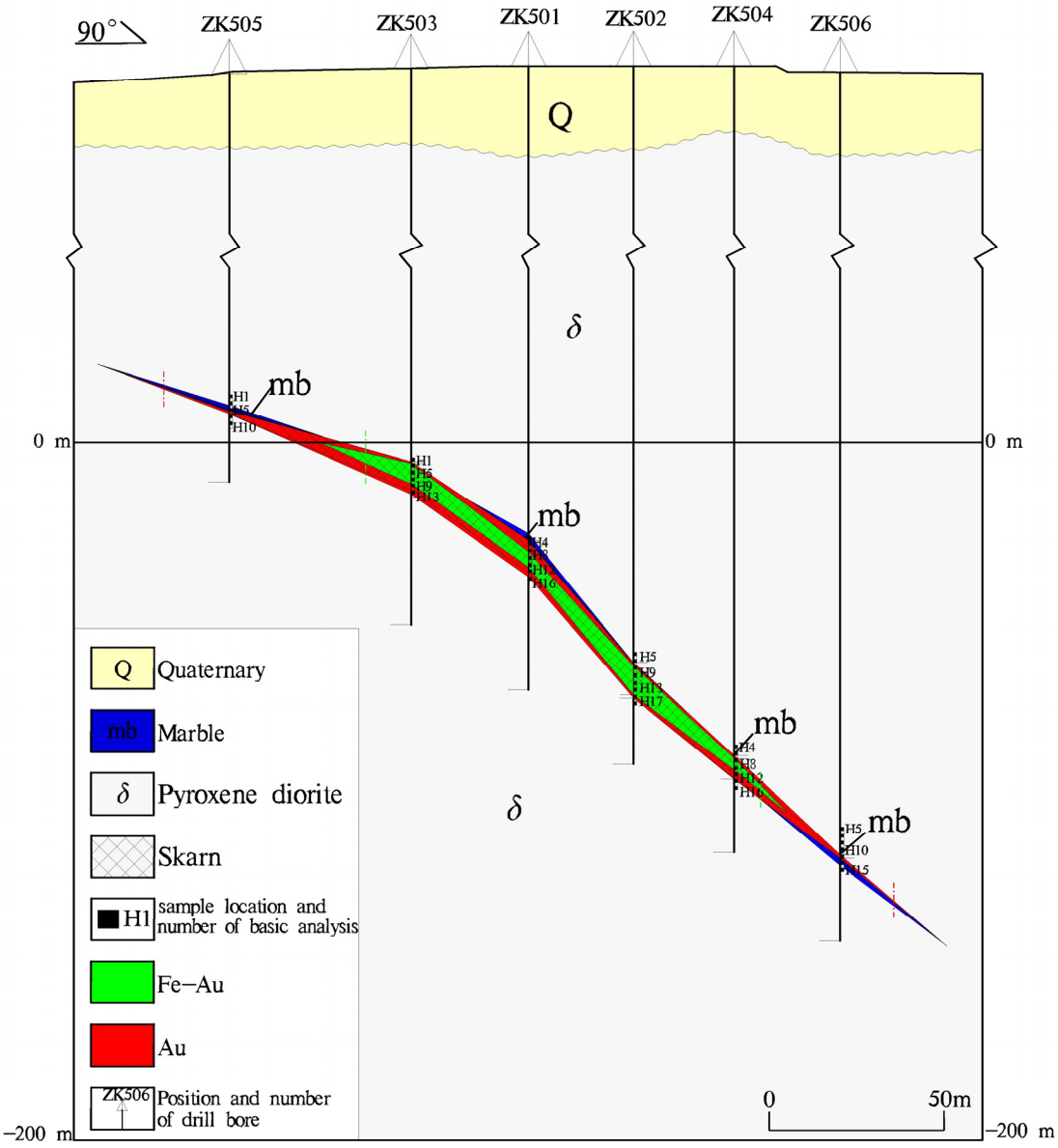

Figure 3. Geological profile of the no.5 exploration line in the Sanchahe mining area.

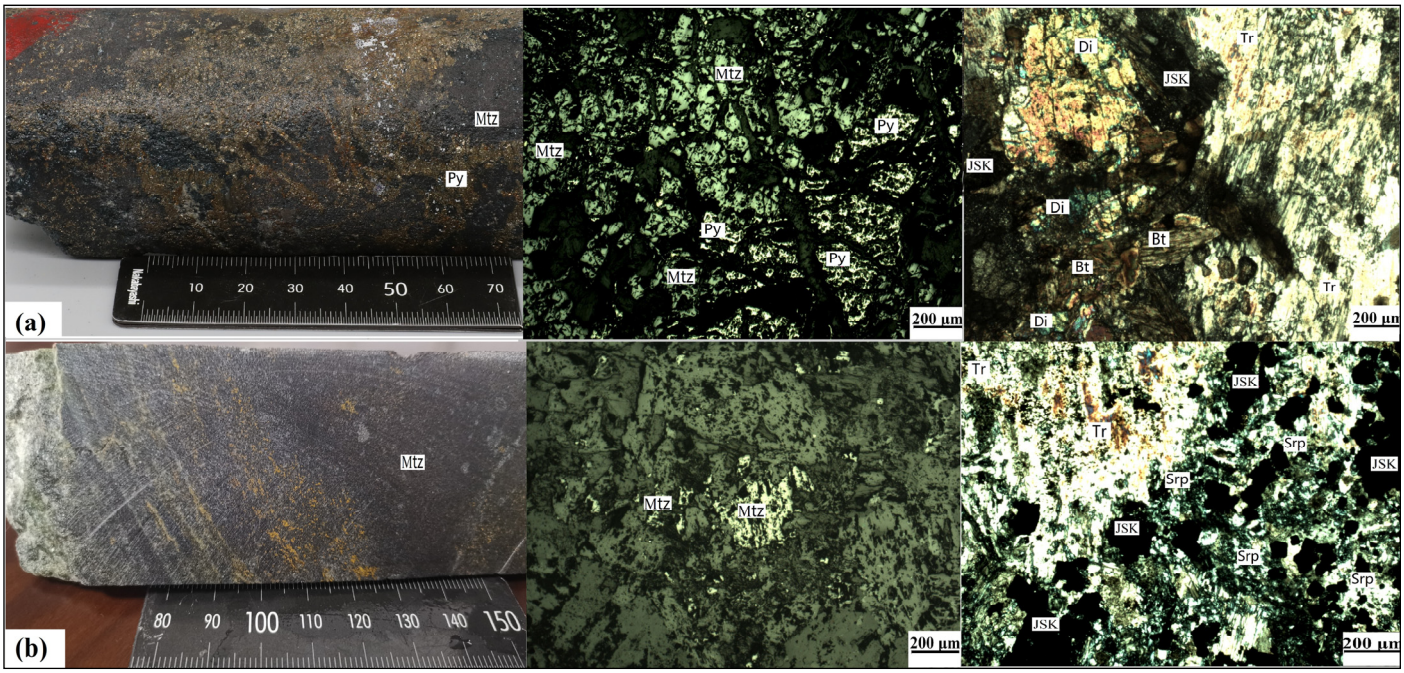

Figure 4. Photographs and microphotographs of pyritized magnetically mineralized skarn (**a**) and magnetically mineralized skarn (**b**). Mtz—magnetite; Py—pyrite; JSK—metal minerals; Di—diopside; Bt—biotite; Tr-tremolite; Srp—serpentine.

3. Sample Description

The pyroxene diorites were collected from the Sanchahe mining area (Figure 2), and are gray–black, residual fine-grained hemihedral texture and massive structure. The samples are fresh and unaltered and contains plagioclases (55–60%), amphiboles (30–35%), pyroxenes (5%), and quartz (<1%) along with accessory zircon and apatite (Figure 5).

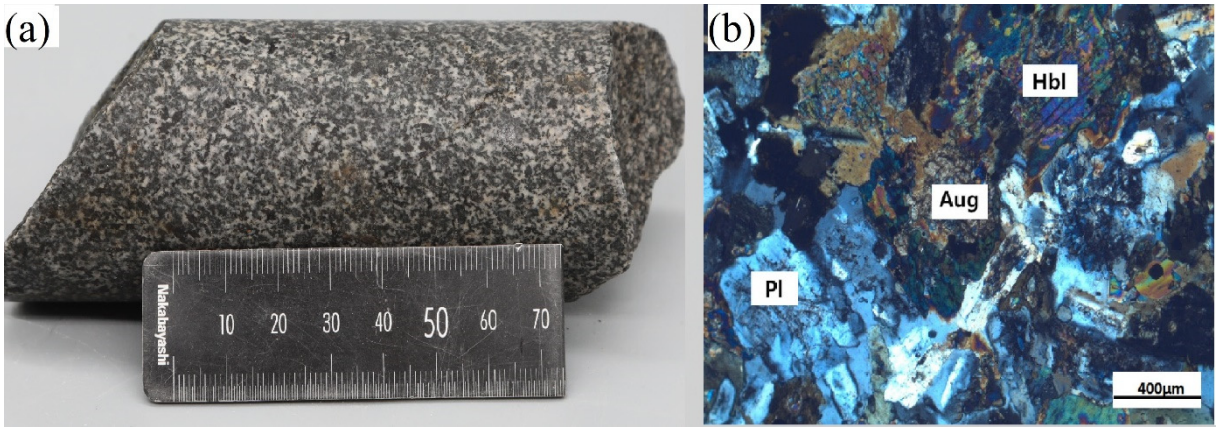

Figure 5. Photographs and microphotographs of the Sanchahe pyroxene diorite. (**a**) The rock is gray-black with granular structure, plagioclase is gray- white, accounting for about 70%, and hornblende is gray-black, accounting for about 30%; (**b**) Plagioclase (Pl, 55–60%): Polysynthetic twin are developed, and the particle size is generally 0.6–1.0 mm. hornblende (Hbl, 30–35%): there are two groups of oblique cleavage, and the particle size is generally 0.4–1.2 mm. Augite (Aug, 0.5%), short diameter, and the particle size is generally 0.1–0.3 mm.

4. Analytical Methods

The zircon U-Pb dating and Lu-Hf isotope samples were taken from the ZK0003 borehole, the whole-rock major and trace elements, and the Sr-Nd-Pb isotope for test samples were taken from the ZK803, ZK004, and ZK005 boreholes.

4.1. Zircon U-Pb Dating and Hf Isotope

The fresh samples without xenoliths (and after removing the weathered surface) were selected for crushing. After the pyroxene diorite was crushed manually, the zircons were separated by gravity separation and electromagnetic separation, and the zircon particles with better crystal shape and transparency were selected under binoculars. Then, they were glued on the glass slide with double-sided tape and collected. The collected zircons were put on the target ring, and after the epoxy resin was injected, it was cooled and polished to expose the zircon surface for the acquisition of transmitted light, reflected light, and cathodoluminescence (CL) images. Zircon U-Pb dating was performed using a combination of NWR 193 nm ArF excimer laser ablation system (Elemental Scientific Lasers, Omaha, NE, USA) and ThermoiCap-RQ quadrupole ICP-MS (Thermo Fisher Scientific, Bremen, Germany). In the experiment, helium was used as the carrier gas for the ablation material, and the laser frequency was 8 Hz, the energy was 5 J/cm^2, the beam spot diameter was 32 μm, and the laser ablation time was 40 s. The test results were processed offline by ICPMSDataCal software (version 10.9, China University of Geosciences, Wuhan, Hubei, China). International standard zircon 91500 was used as the external standard to correct instrumental mass discrimination and elemental fractionation during the ablation and zircon PL was treated as quality control for geochronology (337.13 ± 0.37 Ma). The detailed experimental analysis steps and data processing methods can be found in references [13,14]. Sample processing and analytical testing were performed at Guangzhou Tuoyan Testing Technology Co., Ltd. (Guangzhou, Guangdong, China).

The zircon in situ Lu-Hf isotope test location is the effective point of the previous U-Pb dating. The Neptune multi-receiver inductively coupled plasma mass spectrometer (Thermo Fisher Scientific, Bremen, Germany) equipped with a 193 nm laser was used for the determination (Elemental Scientific Lasers, Omaha, NE, USA). For the detailed test process and analysis steps, please refer to reference [15]. During the analysis, a laser with a frequency of 9 Hz and an energy of 3.5 J/cm^2 ablated the zircons. The ablation diameter was 50 μm, and the ablation time was 40 s. During the testing process, for every five samples of zircon, one standard zircon (including GJ-1, 91500, Plešovice, Mud Tank, Penglai) was tested in turn to check the data quality of the zircon–Hf isotope ratio. For the calculation formula and the Hf isotopic method, please refer to reference [16]. Sample processing and analytical testing were performed at Guangzhou Tuoyan Testing Technology Co., Ltd.

4.2. Geochemistry

Sample processing and the major and trace elements analysis were performed at Guangzhou Tuoyan Testing Technology Co., Ltd. Major elements were determined using X-ray fluorescence spectrometry (XRF, M4 Tornado plus, Bruker, Germany). Trace and rare earth elements were analyzed by an inductively coupled plasma mass spectrometer (ICP-MS). The analytical precision and accuracy of major elements were better than 5%, and the analytical precision and accuracy of trace and rare earth elements were 5% to 10%. The detailed analysis steps of the experiment can be found in reference [17].

The whole-rock Sr-Nd-Pb isotopic analysis was completed at Beijing Zirconium Linghang Technology Co., Ltd. (Beijing, China). The model of the Sr-Nd isotope testing instrument was the thermal ionization mass spectrometer (TIMS-ICPMS). First, we weighed 50–100 mg of rock powder crushed to 200 mesh and placed it in a sample dissolving bomb, and dissolved it with 1.5 mL HF + 1.5 mL HNO_3 at 195 °C for 24 h. Then, we evaporated it to dryness at 115 °C, and added 1 mL HCl. Finally, AG50X8 Rb and Sr were separated by cation exchange resin, and Sm and Nd were separated by HDEHP leaching resin. The measured data of the samples were normalized with $^{86}Sr/^{88}Sr$ = 0.1194 and $^{146}Nd/^{144}Nd$ = 0.7219. The detailed experimental procedures and analysis methods can be found in the literature [17]. For the Pb isotope analysis, we first accurately weighed an appropriate amount (about 100 mg) of the sample into a polytetrafluoroethylene sample dissolution tank, added 2.5 mL of HF, 0.5 mL of HNO_3, and 0.15 mL of $HClO_4$, and placed it on an electric hot plate at 150 °C for one week for dissolving the sample. After the sample was

dissolved, we evaporated the sample solution to dryness, dissolved the sample with 2 mL 3 M HNO_3, centrifuged it for resin separation, used Sr special resin (2 mL) to separate and purify Pb, and used a 3 M HNO_3 and 6 N HCl acid process to separate and purify the Pb sample. During whole process of the lead, the background was less than 200 pg. The Pb isotope ratio was determined by a Triton thermal ionization mass spectrometer (TIMS) (Thermo Fisher Scientific, Bremen, Germany), and the lead isotope was measured using a silica gel emitter and a rhenium metal band, and the measurement temperature was about 1300 °C. The lead's standard material NBS981 was used to monitor the instrument status, and the international standard rock sample BCR-2 (basalt) was used to monitor the separation process during the experiment. The detailed analysis steps of the experiment can be found in reference [18].

5. Results

5.1. Zircon U-Pb Ages

The CL images of zircons from the pyroxene diorites in the Sanchahe area are shown in Figure 6. The sizes of zircon grains are from 70 μm to 270 μm, whereas the shapes of zircons are mainly long or short and columnar. At the same time, the zircons show typical magmatic zonal structures [19]. The contents of Th and U are from 188 ppm to 633 ppm, and from 176 ppm to 456 ppm, respectively. The ratios of Th/U are from 1.0 to 1.4, indicating the features of magmatic zircons [20]. Twenty-five zircons from sample ZK0003B4 were selected for dating, and the data are listed in Table 1. The concordance degree of seven grains was below 90%, and the other eighteen grains yielded an average age of 138.4 ± 1.2 Ma (MSWD = 1.1, n = 18) (Figure 7). This Cretaceous age could represent the emplacement age of the gabbro diorites in the Sanchahe area.

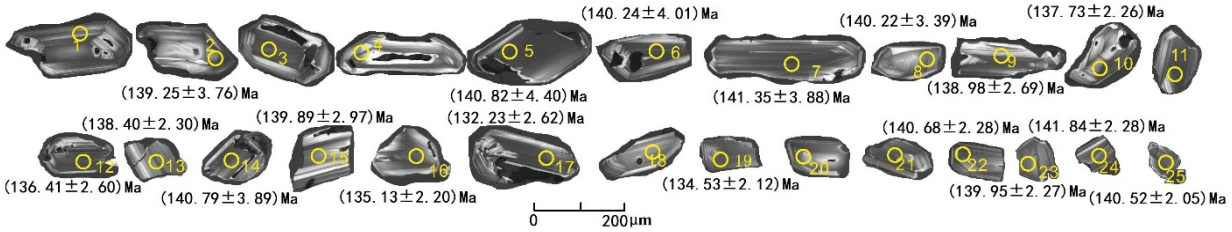

Figure 6. Cathodoluminescence images of zircons of the Sanchahe pyroxene diorite.

Table 1. Analyzed results of LA-ICP-MS zircons U-Pb of the Sanchahe pyroxene diorite.

No.	Th (ppm)	U (ppm)	Th/U	U-Pb Isotopic Ratios						Age (Ma)						
				$^{207}Pb/^{206}Pb$	1σ	$^{207}Pb/^{235}U$	1σ	$^{206}Pb/^{238}U$	1σ	$^{207}Pb/^{206}Pb$	1σ	$^{207}Pb/^{235}U$	1σ	$^{206}Pb/^{238}U$	1σ	Concordance
ZK0003B4-1	265	278	1.0	0.0705	0.0042	0.2054	0.0110	0.0219	0.0006	942.59	122.23	189.67	9.23	139.86	3.54	**69%**
ZK0003B4-2	403	334	1.2	0.0479	0.0024	0.1386	0.0068	0.0218	0.0006	94.54	118.50	131.77	6.10	139.25	3.76	94%
ZK0003B4-3	99	116	0.9	0.1075	0.0120	0.6463	0.1896	0.0378	0.0040	1766.67	206.64	506.18	116.94	239.33	25.07	**28%**
ZK0003B4-4	146	160	0.9	0.0909	0.0066	0.2808	0.0197	0.0230	0.0008	1444.14	138.58	251.29	15.64	146.48	4.86	**47%**
ZK0003B4-5	277	237	1.2	0.0467	0.0028	0.1472	0.0083	0.0221	0.0007	31.58	137.02	139.46	7.35	140.82	4.40	99%
ZK0003B4-6	435	355	1.2	0.0469	0.0026	0.1431	0.0080	0.0220	0.0006	55.65	112.95	135.80	7.09	140.24	4.01	96%
ZK0003B4-7	364	311	1.2	0.0454	0.0023	0.1392	0.0078	0.0222	0.0006	error	-	132.32	6.93	141.35	3.88	93%
ZK0003B4-8	188	176	1.1	0.0507	0.0030	0.1539	0.0088	0.0220	0.0005	227.85	139.80	145.38	7.77	140.22	3.39	96%
ZK0003B4-9	248	232	1.1	0.0507	0.0031	0.1484	0.0075	0.0218	0.0004	233.40	140.72	140.46	6.61	138.98	2.69	98%
ZK0003B4-10	633	456	1.4	0.0486	0.0023	0.1436	0.0058	0.0216	0.0004	127.87	112.95	136.22	5.19	137.73	2.26	98%
ZK0003B4-11	48	90	0.5	0.5532	0.0231	6.4256	0.4872	0.0715	0.0037	4389.82	61.05	2035.78	66.63	445.04	22.32	**−29%**
ZK0003B4-12	435	324	1.3	0.0533	0.0029	0.1569	0.0086	0.0214	0.0004	342.65	124.06	148.00	7.59	136.41	2.60	91%
ZK0003B4-13	332	297	1.1	0.0501	0.0030	0.1456	0.0076	0.0217	0.0004	198.23	145.35	138.06	6.72	138.40	2.30	99%
ZK0003B4-14	581	405	1.4	0.0532	0.0030	0.1553	0.0079	0.0221	0.0006	344.50	125.91	146.57	6.97	140.79	3.89	95%
ZK0003B4-15	206	189	1.1	0.0475	0.0031	0.1422	0.0086	0.0219	0.0005	72.32	148.13	135.04	7.65	139.89	2.97	96%
ZK0003B4-16	588	442	1.3	0.0540	0.0023	0.1550	0.0059	0.0212	0.0003	372.28	96.29	146.28	5.16	135.13	2.20	92%
ZK0003B4-17	541	429	1.3	0.0504	0.0025	0.1421	0.0069	0.0207	0.0004	216.74	116.65	134.88	6.17	132.23	2.62	98%
ZK0003B4-18	104	98	1.1	0.2683	0.0215	1.4524	0.1351	0.0307	0.0012	3295.99	126.54	910.86	55.93	194.67	7.24	**−30%**
ZK0003B4-19	342	393	0.9	0.0483	0.0028	0.1485	0.0071	0.0211	0.0003	122.31	120.35	140.62	6.24	134.53	2.12	95%
ZK0003B4-20	263	239	1.1	0.0819	0.0042	0.2442	0.0118	0.0217	0.0004	1242.59	100.46	221.88	9.63	138.17	2.34	**53%**
ZK0003B4-21	197	142	1.4	0.1766	0.0123	0.7495	0.0609	0.0280	0.0012	2621.30	115.59	567.95	35.32	177.77	7.39	**−5%**
ZK0003B4-22	424	359	1.2	0.0533	0.0026	0.1625	0.0080	0.0221	0.0004	338.95	111.10	152.92	7.02	140.68	2.28	91%
ZK0003B4-23	249	252	1.0	0.0465	0.0027	0.1405	0.0077	0.0219	0.0004	33.43	133.32	133.53	6.84	139.95	2.27	95%
ZK0003B4-24	426	329	1.3	0.0442	0.0021	0.1353	0.0058	0.0222	0.0004	error	-	128.89	5.21	141.84	2.28	90%
ZK0003B4-25	408	380	1.1	0.0517	0.0027	0.1571	0.0077	0.0220	0.0003	272.29	118.50	148.14	6.77	140.52	2.05	94%

Note: The bold is the data of zircon samples with low concordance.

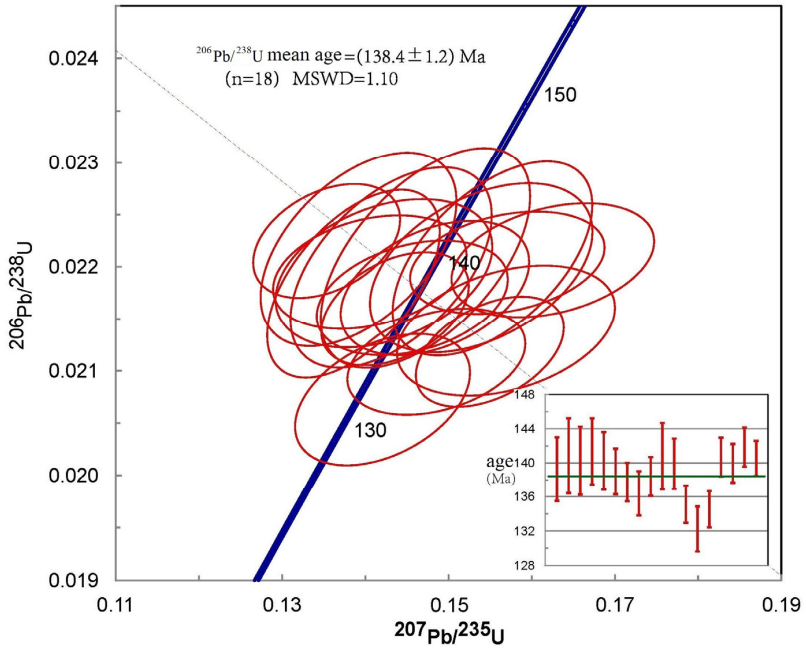

Figure 7. Concordia diagrams showing LA-ICP-MS zircon U-Pb dating for the Sanchahe pyroxene diorite. The red circles are the data U-Pb points. The center of circles are the mean values of the $^{206}Pb/^{238}U$ ratios. The size of circles depends on the errors, and the direction are dependent on the rho. The small vertical red lines represent the $^{206}Pb/^{238}U$ ages of each U-Pb points. The length of each lines depends on the error, and the middle depends on the mean values of the $^{206}Pb/^{238}U$ age.

5.2. Major and Trace Elements

The samples ZK803, ZK004, and ZK005 were selected for major and trace elements analysis in the study. The data are provided in Table 2 and plotted in Figures 8 and 9.

Table 2. Chemical compositions of major elements, trace elements, and REE elements of the Sanchahe pyroxene diorite.

Composition	ZK803	ZK0004	ZK0005	Sapmle	ZK803	ZK0004	ZK0005
SiO_2	59	55	55	Mo	1.2	3.2	2.6
TiO_2	0.7	0.7	0.7	Cd	0.22	0.03	0.03
Al_2O_3	15	15	15	Sn	1.6	3.1	3.0
Fe_2O_3	7.0	8.8	8.9	Sb	0.57	0.33	0.35
MnO	0.1	0.1	0.1	Cs	3.6	2.0	1.9
MgO	5.9	6.5	6.8	Ba	842	816	802
CaO	5.9	6.7	6.6	La	23	21	21
Na_2O	3.5	3.4	3.4	Ce	46	36	38
K_2O	2.4	2.2	2.1	Pr	5.5	5.4	5.6
P_2O_5	0.2	0.3	0.3	Nd	22	23	24
Loss	0.9	0.9	1.2	Sm	4.3	4.5	4.7
Sum	100	100	100	Eu	1.2	1.3	1.4
$K_2O + Na_2O$	5.9	5.6	5.5	Gd	4.0	3.6	3.7
A/CNK	0.8	0.8	0.8	Tb	0.53	0.58	0.61
$Mg^{\#}$	63	60	60	Dy	2.7	3.1	3.1
Na_2O/K_2O	1.5	1.5	1.7	Ho	0.52	0.57	0.57
σ	2.2	2.5	2.5	Er	1.4	1.6	1.6
Li	24	31	29	Tm	0.21	0.21	0.21

Table 2. *Cont.*

Composition	ZK803	ZK0004	ZK0005	Sapmle	ZK803	ZK0004	ZK0005
P	963	1170	1157	Yb	1.3	1.4	1.3
Sc	19	25	24	Lu	0.2	0.2	0.2
Ti	3940	4286	4227	Hf	3.4	2.3	2.3
V	148	164	161	Ta	0.4	0.4	0.3
Cr	334	289	289	Pb	16	13	13
Mn	792	911	908	Th	6.3	2.8	2.9
Co	24	28	28	U	1.8	0.9	0.9
Ni	104	98	93	∑LREE	102	91	94
Cu	21	7.8	12	∑HREE	26	28	26
Zn	78	27	29	∑REE	128	118	120
Ga	21	16	16	Rb/Sr	0.10	0.05	0.04
Ge	1.6	1.0	0.9	Ba/Rb	12	21	22
Rb	68	39	37	Zr/Hf	38	78	87
Sr	668	853	844	La/Sm	5.3	4.6	4.6
Y	15	15	14	Nb/Ta	17	15	15
Zr	129	179	199	$(La/Yb)_N$	12	11	11
Nb	6.7	5.3	4.7	δEu	0.88	0.98	0.96

Note: major elements (%), trace elements and REE elements (ppm).

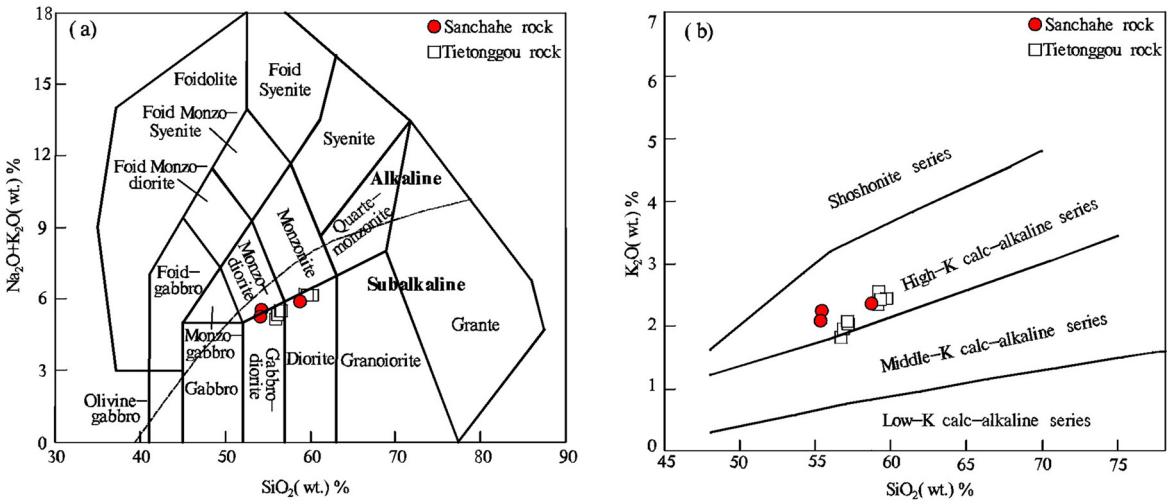

Figure 8. TAS (**a**) and w(K_2O)-w(SiO_2) (**b**) diagram of the Sanchahe pyroxene diorite. (**a**) After [21], (**b**) after [22]; Tietonggou data according to Yang Chenghai [5].

5.2.1. Major Elements

The geochemical data of pyroxene diorites in the Sanchahe area are listed in Table 2. Although some minerals in the samples were altered, the loss (0.9~1.2%, <5%) indicated that the degree of weathering alteration was relatively low and had little effect on the determination of major elements. The samples with SiO_2 contents of 55.3~58.7% had intermediate magmatic characteristics and the contents of Al_2O_3, Na_2O, K_2O and Fe_2O_3 were 15%, from 3.4% to 3.5%, from 2.1% to 2.4%, and from 7.0% to 8.9%, respectively. The contents of MgO were from 5.9% to 6.8% and the values of $Mg^{\#}$ were 60% to 63%, indicating the features of high Mg diorites. Meanwhile, the total alkali contents (K_2O + Na_2O) were 5.5% to 5.9%. The ratios of Na_2O/K_2O were from 1.5% to 1.7%, and the Rittman indexes were from 2.2% to 2.5%, indicating the evolution trend of sub-alkaline series magma. The values of A/CNK were 0.8. Thus, all of the samples were weak peraluminous. The samples are plotted in the field of the diorites in the diagram of total alkali silicon (TAS) (Figure 8a), whereas all of the samples are plotted in the high-K calc-alkaline series field in the SiO_2–K_2O diagram (Figure 8b).

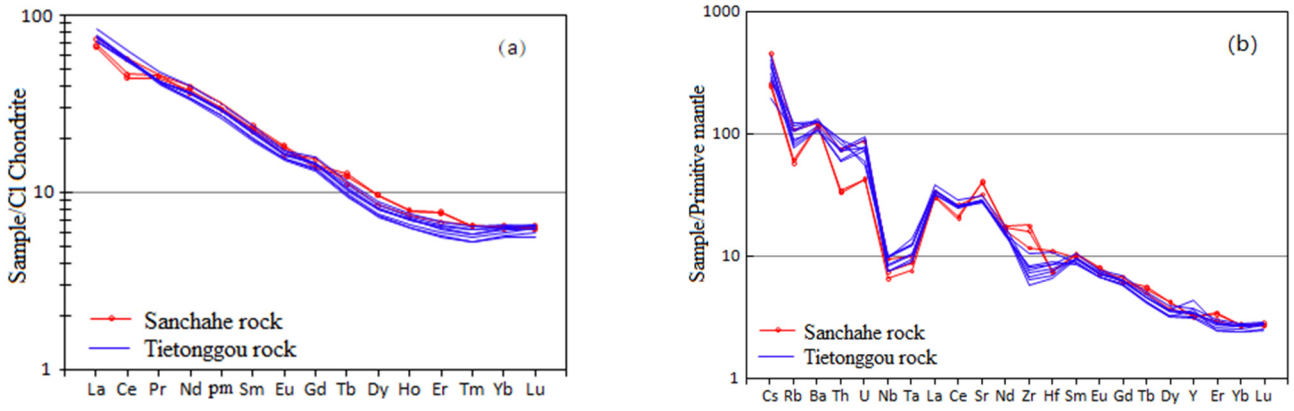

Figure 9. Chondrite normalized rare earth element pattern diagram(**a**) and primitive mantle normalized spider diagram (**b**) of the Sanchahe pyroxene diorite. ((**a**) after Boynton [23]; (**b**) after Sun S S [24]; Tietonggou data according to Yang Chenghai [5]).

5.2.2. Trace Elements

The contents of REE from the samples were from 118 ppm to 128 ppm. Furthermore, the contents of LREEs were from 91 ppm to 102 ppm, and the contents of HREEs were from 26 ppm to 28 ppm. The values of LREE/HREE were from 3.3 to 4.0. The chondrite normalized rare earth element pattern diagram shows that all samples were enriched in LREEs and depleted in HREEs (Figure 9a). The values of δEu were from 0.88 to 0.98 and the samples hada weak negative anomaly of Eu. In the primitive mantle normalized spider diagram (Figure 9b), the samples were enriched in LILEs (Rb, Cs, Ba, Sr), and depleted in HFSEs (Nb, Ta, Zr). The samples had high contents of Sr and Yb: w(Sr) = 668~853 ppm, w(Yb) = 1.3~1.4 ppm. The samples also had high contents of Sc, Cr, Co, and Ni: w(Sc) = 19~24 ppm, w(Cr) = 289~334 ppm, w(Co) = 24~28 ppm, w(Ni) = 93~104 ppm. Furthermore, the values of Nb/Ta and Zr/Hf were from 15 to 17 and from 38 to 87, respectively.

5.3. Sr-Nd-Pb Isotopic Features

The samples ZK002, ZK004 and ZK005 were selected for Sr-Nd-Pb isotope analysis in this study. The whole rock Sr-Nd-Pb isotopic compositions of those samples are listed in Table 3. The contents of Sr were from 692 ppm to 949 ppm and the contents of Nd were from 19 ppm to 20 ppm. Emplacement age of 138.4 Ma were used to calculated $(^{87}Sr/^{86}Sr)_i$ and $(^{143}Nd/^{144}Nd)_i$. The ratios of $^{87}Rb/^{86}Sr$, $^{87}Sr/^{86}Sr$, $^{147}Sm/^{144}Nd$, and $^{143}Nd/^{144}Nd$ were from 0.15642 to 0.27798, from 0.70855 to 0.70946, from 0.11701 to 0.12570, and from 0.51193 to 0.51215, respectively. The ratios of $(^{87}Sr/^{86}Sr)_i$ and $(^{143}Nd/^{144}Nd)_i$ were from 0.70824 to 0.70891, and from 0.51182 to 0.51204, respectively. The values of $\varepsilon_{Nd}(t)$ were from −8.1 to −12.5 and the Nd isotopic model ages (T_{DM2}) were from 1591 Ma to 1950 Ma.

The contents of Pb, Th and U were from 13 ppm to 16 ppm, from 2.8 ppm to 6.3 ppm, and from 0.9 ppm to 1.8 ppm, respectively. Moreover, $^{208}Pb/^{204}Pb$ = 37.206~38.160, $^{207}Pb/^{204}Pb$ = 15.362~15.497, and $^{206}Pb/^{204}Pb$ = 17.055~17.918. Based on the age of 138.4 Ma, the initial ratios of $(^{208}Pb/^{204}Pb)$, $(^{207}Pb/^{204}Pb)$, and $(^{206}Pb/^{204}Pb)$ were from 37.106 to 37.993, from 15.357 to 15.490, and from 16.960 to 17.770, respectively.

5.4. Zircon Hf Isotopes

The sample ZK003 was selected for zircon Hf isotope analysis in the study. The locations of thirteen dating spots were the same or near the zircon U-Pb dating locations (Figure 6). The values of $\varepsilon_{Hf}(t)$ were calculated based on the weighted average age of the samples. The data results have been listed in Table 4. The ratios of $^{176}Lu/^{177}Hf$ are from 0.00109 to 0.00374, with an average value of 0.00200, indicating the limited accumulation of radiogenic Hf after the formation of zircons in the pyroxene diorites. Thus, the values of $^{176}Lu/^{177}Hf$ could represent the original Hf isotopic composition of parent melts from

which zircon crystallize [16,25]. The $(^{176}Hf/^{177}Hf)_i$ values of zircons are 0.28219~0.28249, with an average value of 0.28230, and the $^{176}Yb/^{177}Hf$ values of zircons are 0.04133~0.11775, with an average value of 0.07012. Furthermore, the values of Hf(t) are −17.4~−7.0, with an average value of −13.8. The ages of T_{DM1} are from 1132 Ma to 1573 Ma, whereas the ages of T_{DM2} are from 1634 Ma to 2289 Ma. The values of $f_{Lu/Hf}$ in the range of −0.97 and −0.89 were less than −0.34 of the siliceous magnesian crust [26] and −0.72 of the aluminosilicate crust [27].

Table 3. Whole-rock Sr-Nd-Pb isotopic composition for the pyroxene diorites in the Sanchahe deposit.

Sample No.	ZK002	ZK004	ZK005
Rb(ppm)	66	55	51
Sr(ppm)	692	920.70	949
$^{87}Rb/^{86}Sr$	0.27798	0.17251	0.15642
$^{87}Sr/^{86}Sr$	0.70946	0.70873	0.70855
2σ	0.000006	0.000005	0.000009
$(^{87}Sr/^{86}Sr)_i$	0.70891	0.70839	0.70824
Sm(ppm)	3.8	4.0	4.1
Nd(ppm)	19	19	20
$^{147}Sm/^{144}Nd$	0.11701	0.12570	0.12246
$^{143}Nd/^{144}Nd$	0.51215	0.51193	0.51194
2σ	0.000006	0.000008	0.000007
$(^{143}Nd/^{144}Nd)_i$	0.51204	0.51182	0.51183
εNd(t)	−8.1	−12.5	−12.3
T_{DM} (Ma)	1576	2108	2015
T_{2DM} (Ma)	1591	1950	1928
Pb(ppm)	16	13	13
Th(ppm)	6.3	2.8	2.9
U(ppm)	1.8	0.9	0.9
$^{206}Pb/^{204}Pb$	17.918	17.289	17.055
2σ	0.001	0.001	0.001
$^{207}Pb/^{204}Pb$	15.497	15.405	15.362
2σ	0.001	0.001	0.001
$^{208}Pb/^{204}Pb$	38.160	37.445	37.206
2σ	0.003	0.002	0.002
$(^{208}Pb/^{204}Pb)_i$	37.993	37.351	37.106
$(^{207}Pb/^{204}Pb)_i$	15.490	15.401	15.357
$(^{206}Pb/^{204}Pb)_i$	17.770	17.198	16.960

Table 4. Zircon Lu-Hf isotopic data for the pyroxene diorites in the Sanchahe deposit.

No.	Age (Ma)	$^{176}Yb/^{177}Hf$	2σ	$^{176}Lu/^{177}Hf$	2σ	$^{176}Hf/^{177}Hf$	2σ	$(^{176}Hf/^{177}Hf)i$	εHf(0)	εHf(t)	T_{DM1} (Ma)	T_{DM2} (Ma)
ZK003-2	139.25	0.04133	0.00178	0.00109	0.00014	0.28231	0.00002	0.28231	−16.3	−13.4	1334	2044
ZK003-5	140.82	0.06845	0.00399	0.00178	0.00028	0.28227	0.00003	0.28227	−17.8	−14.8	1416	2136
ZK003-6	140.24	0.09319	0.00155	0.00302	0.00022	0.28250	0.00010	0.28249	−9.8	−7.0	1132	1639
ZK003-8	140.22	0.05652	0.00119	0.00151	0.00007	0.28229	0.00003	0.28229	−17.1	−14.1	1378	2091
ZK003-9	138.98	0.04196	0.00069	0.00117	0.00005	0.28231	0.00003	0.28231	−16.4	−13.5	1340	2049
ZK003-10	137.73	0.04563	0.00168	0.00127	0.00008	0.28230	0.00003	0.28230	−16.7	−13.8	1357	2071
ZK003-13	138.40	0.06540	0.00063	0.00184	0.00009	0.28227	0.00003	0.28227	−17.7	−14.9	1417	2136
ZK003-14	140.79	0.09679	0.01139	0.00316	0.00125	0.28220	0.00004	0.28219	−20.2	−17.4	1573	2297
ZK003-15	139.89	0.06300	0.00090	0.00162	0.00007	0.28229	0.00003	0.28229	−17.0	−14.1	1379	2088
ZK003-17	132.23	0.11775	0.00334	0.00374	0.00036	0.28223	0.00004	0.28222	−19.1	−16.6	1553	2237
ZK003-19	134.53	0.06928	0.00106	0.00235	0.00014	0.28226	0.00004	0.28226	−18.0	−15.2	1448	2157
ZK003-23	139.95	0.06509	0.00144	0.00200	0.00015	0.28241	0.00003	0.28240	−12.9	−10.0	1227	1831
ZK003-25	140.52	0.08787	0.00073	0.00273	0.00008	0.28229	0.00003	0.28228	−17.2	−14.4	1430	2105

6. Discussion

6.1. Geochronology

The Sanchahe Fe-Au deposit is a typical skarn deposit. Its mineralization is likely linked with the pyroxene diorites in the Sanchahe area. However, the chemical reaction strongly occurred between the pluton and surrounding rocks and promoted the exchange

of Si, Al, Ca and Mg during the forming of skarn deposits. Thus, the forming age of the pluton could probably represent the forming age of the deposit. The hidden pluton of Sanchahe is located to the south of the Tietonggou complex pluton and is considered part of the Tietonggou complex pluton. However, many studies have been carried out on the geochronology of the Tietonggou complex. Considering that the Jurassic Santai group was intruded by the Tietonggou complex, the forming age of the Tietonggou complex pluton was defined as the Early Cretaceous. Xu et al. [28] reported the biotite $^{40}Ar/^{39}Ar$ age of 133 Ma from pyroxene diorites. This age is consistent with the biotite $^{40}Ar/^{39}Ar$ age from the diorites reported by Wang et al. [29]. In addition, Yang et al. [5] reported the Early Cretaceous weighted mean ages (~134 Ma) of zircons with the method of LA-ICP-MS. The LA-ICP-MS zircon U-Pb dating of Sanchahe pyroxene diorites in Laiwu has been carried out in this paper. Our analyzed zircon grains are characterized by long or short columnar shapes, high Th/U ratios (1.0 to 1.4), low LREE/HREE ratios (>3), and the weak negative anomaly of Eu, indicating a magmatic origin. The sample yields a weighted mean age of 138.4±1.2 Ma, indicating the emplacement age of Sanchahe pluton is the Early Cretaceous. Considering the close temporal and spatial distribution relationships between the pluton and the skarn deposits, the forming age of Fe-Au skarn deposits is probably a little later than the forming age of the emplacement age of Sanchahe pluton. However, the emplacement age in this paper is a little older but close to the previously reported ages and is consistent with the ages reported in Jinan, Laiwu, Jinling, Tiezhai, and Yiyuan [30–34]. Based on the above chronological data, it is deemed that the emplacement age of the pluton is consistent with the age of large-scale magmatic events under the lithosphere thinning tectonic setting of the North China Craton.

6.2. The Nature of Source and Petrogenesis

High MgO, Cr, Sc, Co, and Ni contents and high $Mg^{\#}$ values of our analyzed samples collectively indicate the Sanchahe pyroxene diorites were primarily derived from mantle source [35]. This view is further supported by their high Nb/Ta ratios (15 to 17) and Zr/Hf ratios (38 to 87), which are strongly resembling those of mantle-derived melts (Nb/Ta: 18; Zr/Hf: 36), but distinctly higher than those of crustal-derived magmas (Nb/Ta: 11; Zr/Hf: 11) [36]. The $f_{Lu/Hf}$ values (−0.89~−0.97) of our analyzed samples are much lower than those of the ferromagnetic crust(−0.34) and aluminosilicate crust(−0.72) [26,27]. This feature implies the Sanchahe pyroxene diorite originated from mantle.

The relatively low εHf(t) values, LREE and LILE enrichment characteristics of the Sanchahe pluton are very similar to the crustal source material composition, indicating that the source material may be the crustal source or mantle source that underwent subduction and metasomatism enrichments. Experiments have shown that the products of the partial melting of the crust are generally (high-K) calc-alkaline series magma [37], which is consistent with the characteristics of high-K calc-alkaline series pyroxene diorites in the Sanchahe area. Therefore, the Sanchahe pyroxene diorites magma source may have the addition of crustal materials. In addition, low Sm/Nd ratios (0.2) and the geochemical features of pyroxene diorites further indicate the existence of crustal materials in the magma source or during the magmatic evolution process. Furthermore, the high initial $^{87}Sr/^{86}Sr$ values (0.70824~0.70891) and low $\varepsilon_{Nd}(t)$ values (from −8.1 to −12.5) indicate the existence of crustal material. The lithospheric mantle metasomatism by melting material of the subducted oceanic plate is excluded, since the latter has a relatively low initial $^{87}Sr/^{86}Sr$ value and a relatively high εNd(t) value [38]. The $^{176}Hf/^{177}Hf$ of zircons are from 0.28220 to 0.28250, whereas the values of $\varepsilon_{Hf}(t)$ are in the range of −7.0 and −17.4. All of the spots are plotted between the lower crust and chondrite evolution line in Figure 10a and are plotted between the crust and chondrite evolution line in Figure 10b. However, the $\varepsilon_{Hf}(t)$ values are not consistent with the $\varepsilon_{Hf}(t)$ values($\varepsilon_{Hf}(t) > 0$) [39] of the magma from the partial melting of the oceanic crust. At the same time, the Nd two-stage model ages are from 1591 to 1950 Ma, whereas the zircon Hf two-stage model ages are from 1639 Ma to 2297 Ma.

These models ages imply that the source or evolutionary process of primitive magma could involve ancient crust materials.

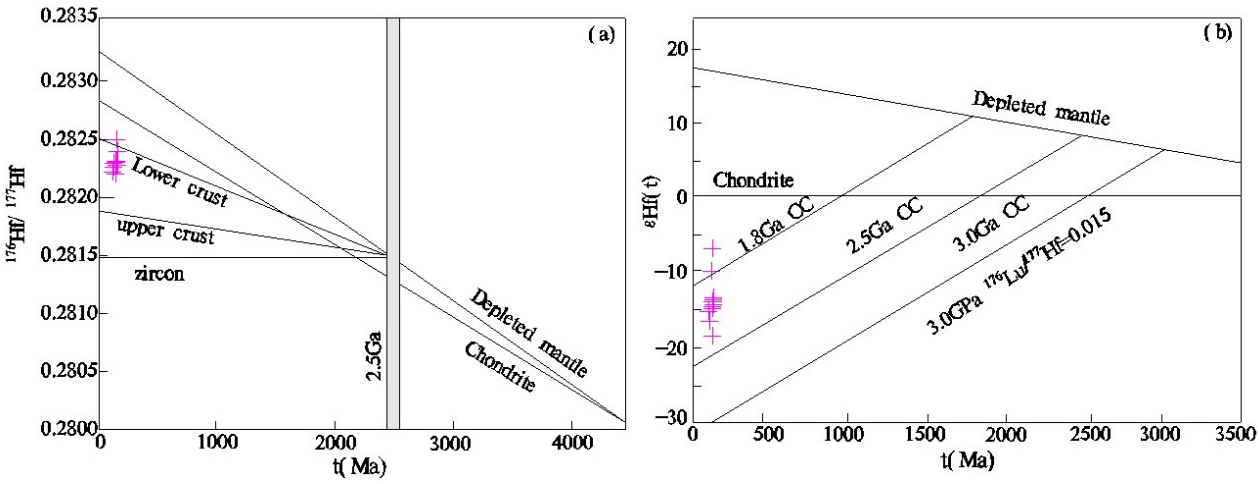

Figure 10. Hf isotopic composition of zircon (adapted from [26]). (**a**) The diagrams of zircon ages vs. $^{176}Hf/^{177}Hf$ for the pyroxene diorite, (**b**) The diagrams of zircon ages vs. εHf(t) for the pyroxene diorite.

Crustal materials modified the nature of the lithosphere mantle but there is still a problem as to whether the crust materials are from the upper crust or the lower crust. The $(^{206}Pb/^{204}Pb)_i$ 16.96~17.77 and $(^{207}Pb/^{204}Pb)_i$ 15.36~15.49 of the samples are similar to those of the lower crust in the North China Craton ($^{206}Pb/^{204}Pb$ = 14.30~17.80, $^{207}Pb/^{204}Pb$ = 14.8~15.5) [40] of the lower crust in the North China Craton. The initial $^{87}Sr/^{86}Sr$ values are from 0.70824 to 0.70891, whereas the $\varepsilon_{Nd}(t)$ values are from −8.1 to −12.5. In the diagrams of $(^{87}Sr/^{86}Sr)_i$ and $\varepsilon_{Nd}(t)$, all of the samples are plotted in the mantle evolution zone (Figure 11). Furthermore, the Nd T_{DM1} ages are from 1576 Ma to 2108 Ma, similar to the ages of the lower crust in the North China Craton. Thus, we conclude that the crustal materials in the mantle were from the lower crust.

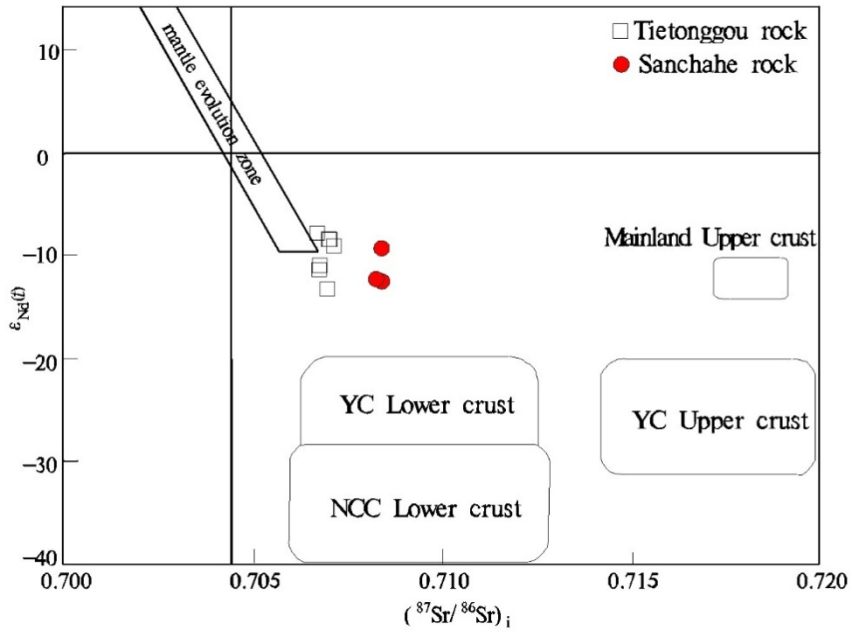

Figure 11. Initial $(^{87}Sr/^{86}Sr)_i$ vs. $\varepsilon_{Nd}(t)$ diagram for the Sanchahe pyroxene diorite. (Tietonggou data according to reference [5]).

There are two main mechanisms for the transformation of the lithospheric mantle by lower crustal materials, including (1) the transformation by crustal materials occurring in the magma source area [38], and (2) the assimilation and contamination by continental crust materials during the process of magma ascending and emplacement [41,42]. Essentially, the former mechanism occurs in the magma source and finally forms a homogeneous chemical system. However, the other mechanism occurred at the depth of crust when mantle-derived magma rises and invaded the lower crust. As a result, the composition of magma was changed significantly [43]. Furthermore, the high $^{87}Sr/^{86}Sr$ values and low $\varepsilon_{Nd}(t)$ values indicate the continental crusts were mixed in the magma source. In addition, there are no obvious linear relationships between $\varepsilon_{Nd}(t)$ and SiO_2 and between $(^{87}Sr/^{86}Sr)_i$ and SiO_2 (Figure 12), indicating limited crustal contamination. Involvement of crustal materials in the formation of Sanchahe pyroxene diorites mainly occurred in its mantle source.

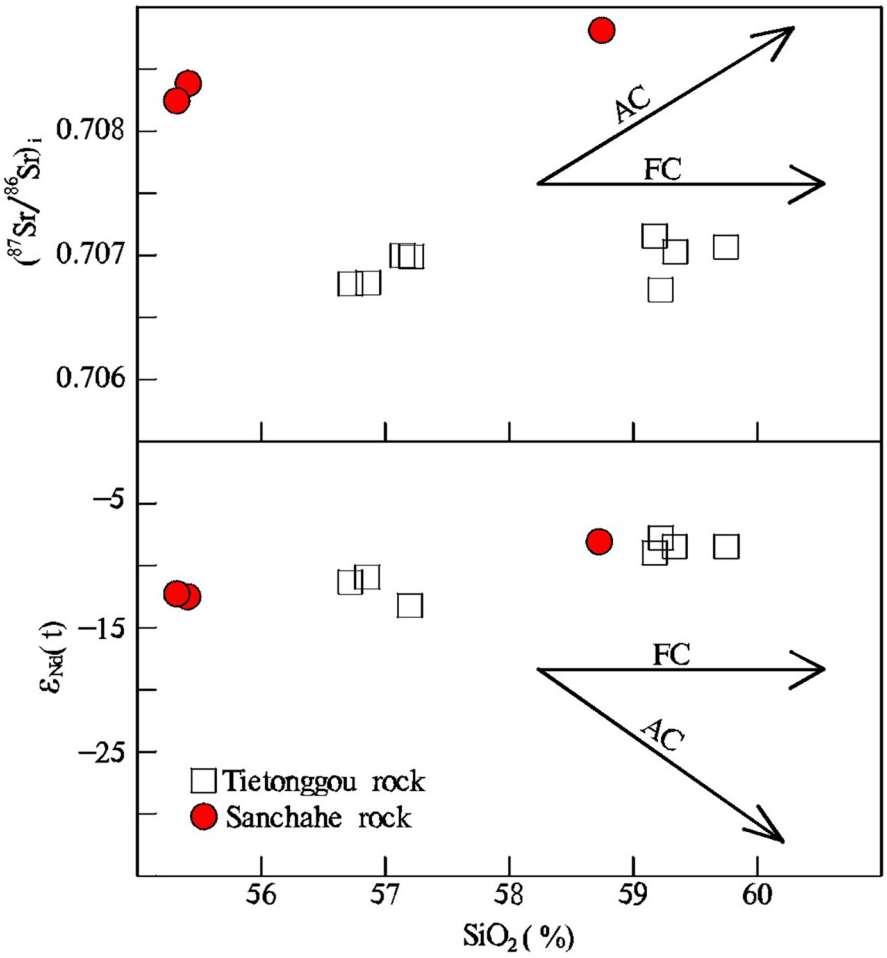

Figure 12. $(^{87}Sr/^{86}Sr)_i$ vs. SiO_2 and $\varepsilon_{Nd}(t)$ vs. SiO_2 for the Sanchahe pyroxene diorites. FC, fractional crystallization; AC, assimilation and contamination. (Tietonggou data according to [5]).

The origin of the continental crust that modified the lithospheric mantle is still under hot debate. Theories include: (1) the delaminated lower crust of the North China Craton, (2) the subducted crust of South China, and (3) the Pacific Ocean crust. High $^{87}Sr/^{86}Sr$ values and low $\varepsilon_{Nd}(t)$ values of samples in this paper are different from the ones of rocks forming in the oceanic crust subduction, suggesting the crust is not the subducted oceanic crust. Pb isotope have been demonstrated as a useful tool to identify the contribution of Yangtze Craton and North China Craton, as they poses specific Pb isotope. The Pb isotope of Tietonggou pluton samples are mostly plotted in the area of North China Craton, with several samples plot in the overlap area between Yangtze Craton and the North China Craton (Figure 13), suggesting crustal material modified lithosphere mantle source of

Sanchahe pluton were dominated by lower crust of North China Craton with minor, if any, lower crust of the Yangtze Craton.

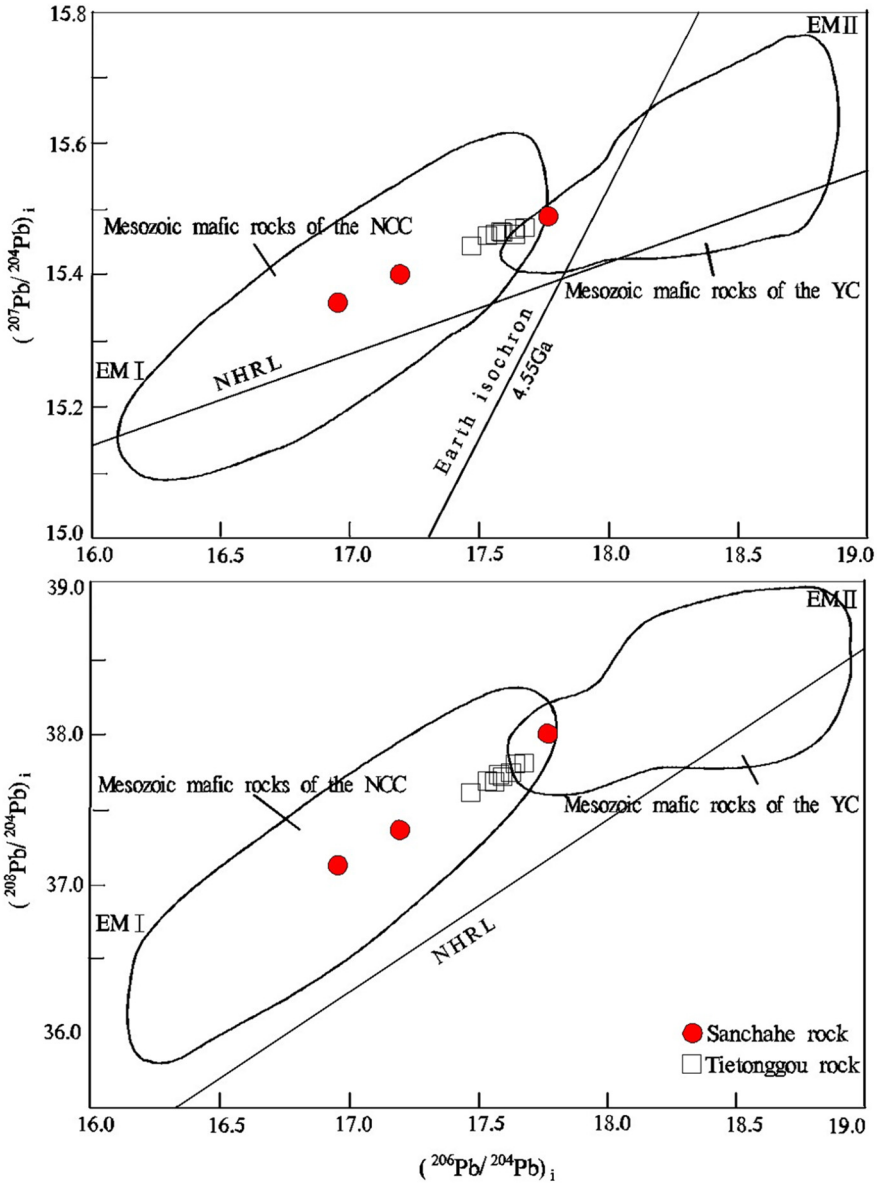

Figure 13. Pb isotopic compositions of the Sanchahe pyroxene diorite (Tietonggou data according to [5]). NHRL, Northern Hemisphere Reference Line.

Research has shown that Rb, Sr, and Ba have great compatibility in amphibole, whereas Rb and K have greater compatibility in phlogopite [44]. Thus, the ratios of Ba/Rb and Rb/Sr could indicate whether the melt source contains amphibole (Ba/Rb > 20, Rb/Sr < 0.1) or phlogopite (Ba/Rb < 20, Rb/Sr > 0.1). The ratios of Rb/Sr and Ba/Rb are from 0.04 to 0.10, and from 12 to 22, respectively. These ratios indicate that amphiboles play an important role and phlogopite plays a secondary role during the formation process of magma melting (Figure 14). Furthermore, the amphiboles and phlogopites provide the most incompatible elements for the refractory ancient lithospheric mantle. In a word, the pyroxene diorites are probably the result of partial melting of mantle peridotite with amphibole and phlogopite.

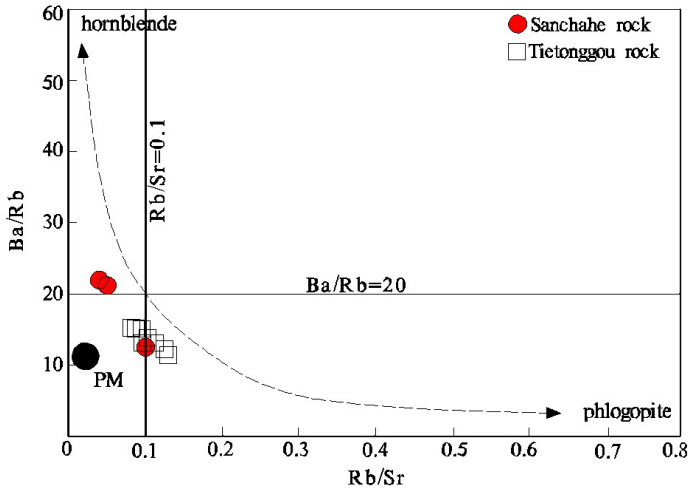

Figure 14. Diagram of w(Ba)/w(Rb)-w(Rb)/w(Sr) of Sanchahe pyroxene diorites (Tietonggou data according to reference [5]).

6.3. Tectonic Setting

The Early Cretaceous emplacement age (138.4 ± 1.2 Ma) of pyroxene diorites in the Sanchahe area is consistent with the ages of Early Cretaceous magmatic activities distributed widely in the North China Craton and has similar geochemistry and Sr-Nd-Pb-Hf isotopic characteristics, suggesting that the Early Cretaceous magmatic activities formed in the same tectonic setting. The Early Cretaceous igneous rocks are a set of bimodal rock assemblages in the eastern North China Craton [45]. The emplacement ages of bimodal rocks are contemporaneous with the peak time of lithospheric thinning in the eastern North China Craton and are also consistent with the forming ages of the metamorphic core complex, extensional sedimentary basins, A-type granites, and alkaline magmatic rocks [46–48], suggesting they formed in an extensional tectonic setting. The Sanchahe pyroxene diorites temporally coincident with widespread bimodal magmatism, rift basin development, and exhumation of metamorphic core complexes, combined marking the peak period of the late Mesozoic large-scale lithospheric thinning in the North China Craton [49,50]. Previous studies suggested that the lithospheric thinning of the North China Craton in the Late Mesozoic was caused by the rollback subduction of the Paleo-Pacific plate towards Eurasia [51,52].

We suggest that the Sanchahe pyroxene diorite was a product of lithospheric destruction of the NCC, which was ultimately triggered by westward subducting paleo-pacific plate. Delamination of lower crust enriched and hydrated the ancient sub-continental lithospheric mantle beneath the Laiwu area. Retreat of the subducting lithospheric plate was accompanied by up welling of hot asthenosphere, leading to extensive partial melting of the fertile mantle lithosphere and formation of voluminous hydrous basaltic magmas. Such basaltic magmas ascent with intense differentiation and fractional crystallization eventually yield intermediate melts from which the Sanchahe pyroxene diorite formed.

7. Conclusions

The emplacement age of pyroxene diorites in the Sanchahe area is 138.4 ± 1.2 Ma, belonging to the Early Cretaceous, and is consistent with the ages of diorite rocks in western Shandong province, whereas the forming age of the Fe-Au deposit was later than the emplacement age of the pluton.

The pyroxene diorites have high $Mg^{\#}$, and all of the samples are characterized by high LREEs/HREEs ratios with enrichment in LILEs but depletion in HFSEs. The Sr-Nd-Pb-Hf isotopic features indicate that the magma source of the pyroxene diorites could be partial melting of the enriched lithospheric mantle dominated by amphibole and reformed

by the delaminated crust of the North China Craton and the subduction plate of the Yangtze Craton.

The Early Cretaceous pyroxene diorites formed in an extensional tectonic setting of the eastern North China Craton. The rollback subduction of the Pacific plate is probably the genetic mechanism for the extensional tectonic setting. The Sanchahe pyroxene diorite was a product of lithospheric destruction of the NCC.

Author Contributions: Conceptualization, M.M.; sampling and experiments, C.T., M.M., Q.F., J.L. and C.T.; data analysis and figures, C.Z., Y.L. (Yadong Li) and Y.L. (Yankui Liu); writing—original draft preparation, M.G.; writing—review and editing, M.M., S.L. and J.G. All authors have read and agreed to the published version of the manuscript.

Funding: This research was supported by the Youth Fund and Open Fund of No. 1 Institute of Geology and Mineral Resources of Shandong Province (QN202003, 2021DW03) and Natural Science Foundation of Shandong Province (ZR2019PD010).

Data Availability Statement: The data used to support the findings of this study are included within the article.

Acknowledgments: Thanks to Kunfeng Qiu from the China University of Geosciences (Beijing) for his valuable opinions and suggestions in the writing process. We are also grateful to the academic editor and anonymous reviewers, whose constructive suggestions greatly improved our manuscript.

Conflicts of Interest: The authors declare no conflict of interest.

References

1. Song, M.C.; Xue, G.Q.; Liu, H.B.; Li, Y.X.; He, C.Y.; Wang, H.J.; Wang, B.; Song, Y.X.; Li, S.Y. A Geological-Geophysical Prospecting Model for Deep-Seated Gold Deposits in the Jiaodong Peninsula, China. *Minerals* **2021**, *11*, 1393. [CrossRef]
2. Meinert, L.D.; Dipple, G.M.; Nicolescu, S. World skarn deposits. *Econ. Geoligy* **2005**, *100th Anniversary Volume*, 236–299.
3. Chang, Z.S.; Shu, Q.H.; Meinert, L.D. Skarnde posits of China. *Econ. Geol. Special* **2019**, *22*, 189–234.
4. Xu, W.L.; Wang, D.Y.; Gao, S.; Lin, J.Q. Discovery of dunite and pyroxenite xenoliths in Mesozoic diorite at Jinling, western Shandong and its significance. *Chin. Sci. Bull.* **2003**, *48*, 1599–1603. [CrossRef]
5. Yang, C.H.; Xu, W.L.; Yang, D.B.; Liu, C.C.; Liu, X.M.; Hu, Z.C. Petrogenesis of the Mesozoic high-Mg diorites in west Shandong: Evidence from chronology and petro-geochemistry. *Earth Sci.-J. China Univ. Geosci.* **2005**, *16*, 297–308.
6. Lan, T.G.; Fan, H.R.; Santosh, M.; Hu, F.F.; Yang, K.F.; Yang, Y.H.; Liu, Y.S. Crust-Mantle Interaction Beneath the LuxiBlock, Eastern North China Craton: Evidence from Coexisting Mantle and Crust-Derived Enclaves in a Quartz Monzonite Pluton. *Lithos* **2013**, *177*, 1–16. [CrossRef]
7. Yang, Q.L.; Zhao, Z.F.; Zheng, Y.F. Modification of subcontinental lithospheric mantle above continental subduction zone: Constraints from geochemistry of Mesozoic gabbroic rocks in southeastern North China. *Lithos* **2012**, *146*, 164–182. [CrossRef]
8. Li, M.X.; Wang, F.Y.; Ding, X. Cretaceous ridge subduction along the lower Yangtze River belt, eastern China. *Econ. Geol.* **2009**, *104*, 303–321.
9. Liu, S.; Li, S.G.; He, Y.S. Geochemical contrasts between early Cretaceous ore-bearing and ore-barren high-Mg adakites in central-eastern China: Implications for petrogenesis and Cu-Au mineralization. *Geochim. Cosmochim. Acta* **2010**, *74*, 7178. [CrossRef]
10. Zhao, G.C.; Sun, M.; Wilde, S.A.; Li, S.Z. Late Archean to Paleoproterozoic evolution of the North China Craton:key issues revisited. *Precambrian Res.* **2005**, *136*, 177–202. [CrossRef]
11. Zhang, H.F.; Sun, M.; Zhou, X.H.; Ying, J.F. Geochemical Constraints on the Origin of Mesozoic Alkaline Intrusive Complexes from the North China Craton and Tectonic Implications. *Lithos* **2005**, *69*, 297–317. [CrossRef]
12. Lan, T.G.; Fan, H.R.; Hu, F.F.; Tomkins, A.G.; Yang, K.F.; Liu, Y.S. Multiple Crust-mantle Interactions for the Destruction of the North China Craton: Geochemical and Sr-Nd-Pb-Hf Isotopic Evidence from the Longbaoshan Alkaline Complex. *Lithos* **2012**, *122*, 87–106. [CrossRef]
13. Yuan, H.L.; Gao, S.; Liu, X.M.; Li, H.M.; Detlef, G.; Wu, F.Y. Accurate U-Pb age and trace element determination of zircon by laser ablation-inductively coupled plasma-mass spectrometry. *Geostand. Geoanalytical Res.* **2004**, *28*, 353–370. [CrossRef]
14. Liu, Y.S.; Hu, Z.C.; Zong, K.Q.; Gao, C.G.; Gao, S.; Xu, J.; Chen, H.H. Reappraisement and refinement of zircon U-Pb isotope and analyses by LA-ICP-MS. *Chin. Sci. Bull.* **2010**, *55*, 1535–1546. [CrossRef]
15. Meng, F.Y.; Zhao, Z.D.; Zhu, D.C. Late Cretaceous Magmatism in Mamba Area, Central Lhasa Subterrane: Products of Back-Arc Extension of Neo-Tethyan Ocean. *Gondwana Res.* **2014**, *26*, 505–520. [CrossRef]
16. Wu, F.Y.; Han, R.H.; Yang, J.H.; Wilde, S.A.; Zhai, M.G.; Park, S.C. Initial constraints on the timing of granitic magmatism in North Korea using U-Pb zircon geochronology. *Chem. Geol.* **2007**, *238*, 232–248. [CrossRef]

17. Ling, W.L.; Duan, R.C.; Xie, X.J. Contrasting geochemistry of the Cretaceous volcanic suites in Shandong province and its implications for the Mesozoic lower crust delamination in the eastern North China craton. *Lithos* **2009**, *113*, 640–658. [CrossRef]
18. Wang, L.Q.; Tang, J.X.; Bagas, L.; Wang, Y.; Lin, X.; Li, Z.; Li, Y.B. Early Eocene Longmalaskam Pb-Zn-Cu deposit in Tibet, China: Geochemistry, fuid inclusions, and H-O-S-Pb isotopic compositions. *Geol. Rev.* **2017**, *88*, 99–115. [CrossRef]
19. Koschek, G. Origin and significance of the SEM cathodoluminescence from zircon. *J. Microsc.* **1993**, *171*, 223–232. [CrossRef]
20. Hoskin, P.W.O.; Black, L.P. Metamorphic zircon formation by solid-state recrystallization of protolith igneous zircons. *J. Metamorph. Geol.* **2000**, *18*, 423–439. [CrossRef]
21. Chu, X.; Sun, J.; Sun, F.; Mei, Y.; Liu, Y.; Men, L.; Zhao, K.; Zhang, X. Petrogenesis of the Early Cretaceous Hongshan Complex in the Southern Taihang Mountains: Constraints from Element Geochemistry, Zircon U-Pb Geochronology and Hf Isotopes. *Minerals* **2021**, *11*, 1111. [CrossRef]
22. Qin, J.; Wang, D.; Chen, Y. Geochemical and Geochronological Constraints on a Granitoid Containing the Largest Indosinian Tungsten(W) Deposit in South China(SC): Petrogenesis and Implications. *Minerals* **2022**, *12*, 80. [CrossRef]
23. Boynton, W.V. *Geochemistry of the Rare Earth Elements: Meteorite Studies//Henderson, P.Rare Earth Element Geochemistry*; Elsevier: Amsterdam, The Netherlands, 1984.
24. Sun, S.S.; Mcdonough, W.F. Chemiscal and Isotopic Systematics of Oceanic Basalts; Implications for Mantle Composition and Processes. *Geol. Soc. Lond. Spec. Publ.* **1989**, *42*, 313–345. [CrossRef]
25. Kinny, P.D.; Compston, W.; Williams, I.S. A Reonnaissance Ion-Probe Study of Hafnium Isotopes in Zircons. *Geochim. Cosmochim. Acta* **1991**, *55*, 849–859. [CrossRef]
26. Vervoort, J.D.; Blichert-Toft, J. Evolution of the Depleted Mantle: Hf Isotope Evidence from Juvenile Rocks through Time. *Geochim. Cosmochim. Acta* **1999**, *63*, 533–556. [CrossRef]
27. Amelin, Y.; Lee, D.C. Halliday Nature of the Earth's Earliest Crust from Hafnium Isotopes in Single Detrital Zircons. *Nature* **1999**, *399*, 252–255. [CrossRef]
28. Xu, W.L.; Wang, D.Y.; Wang, Q.H.; Pei, F.P.; Lin, J.Q. $^{40}Ar/^{39}Ar$ dating of hornblende and biotite in Mesozoic intrusive complex from the North China Block: Constraints on the time of lithospherk thinning. *Geochemistry* **2004**, *33*, 221–231. (In Chinese)
29. Wang, D.Y.; Xu, W.L.; Lan, X.; Wang, Q.H. Petrogenesis of Pyroxenite Xenoliths in Mesozoic Gabbro-Diorite from Western Shandong Province, China. *J. Jiling Univ.* **2004**, *34*, 167–173. (In Chinese)
30. Xu, Y.G.; Huang, X.L.; Ma, J.L.; Wang, Y.B.; Iizuka, Y.; Xu, J.F.; Wang, Q.; Wu, X.Y. Crust-mantle interaction during the tectono-thermal reactivation of the North China Craton: Constraints from SHRIMP zircon U-Pb chronology and geochemistry of Mesozoic plutons from western Shandong. *Contrib. Mineral. Petrol.* **2004**, *147*, 750–767. [CrossRef]
31. Duan, Z.; Li, J.W. Zircon and titanite U-Pb dating of the Zhangjiawa iron skarn deposit, Luxi district, North China Craton: Implications for a craton-wide iron skarn mineralization. *Ore Geol. Rev.* **2017**, *89*, 309–323. [CrossRef]
32. Jin, Z.L.; Zhang, Z.C.; Hou, T.; Santosn, M.; Liu, H. Genetic relationship of high–Mg dioritic pluton to iron mineralization: A case study from the Jinling skarn–type iron deposit in the North China Craton. *J. Asian Earth Sci.* **2015**, *113*, 957–979. [CrossRef]
33. Duan, Z.; Gleeson, S.A.; Gao, W.S. Garnet U-Pb dating of the Yinan Au-Cu skarn deposit, Luxi district, North China Craton: Implications for district-wide coeval Au-Cu and Fe skarn mineralization. *Ore Geol. Rev.* **2020**, *118*, 103310. [CrossRef]
34. Xie, Q.; Zhang, Z.; Hou, T.; Santosh, M.; Jin, Z.L.; Han, L.; Cheng, Z.G. Petrogenesis of the Zhangmatun Gabbro in the Jinan Complex, North China Craton: Implications for Skarn-Type Iron Mineralization. *J. Asian Earth Sci.* **2015**, *113*, 197–1217. [CrossRef]
35. Rapp, R.P.; Watson, E.B. Dehydration melting of metabasalt at 8~32kbar:Implications for continental growth and crust-mantle recycling. *J. Petrol.* **1995**, *36*, 891–931. [CrossRef]
36. Green, T.H. Significance of Nb/Ta as an Indicator of Geochemical Processes in the Crust-Mantle System. *Chem. Geol.* **1995**, *120*, 347–359. [CrossRef]
37. Liu, Y.J.; Liu, B.Q.; Feng, Z.Q.; Wen, Q.B.; Li, W.M.; Zhang, T.; Li, X.Y.; Du, B.Y. SIMS Zircon U-Pb Age, Petrogeochemistry and Its Tectonic Implication of Laodaokou Diorite in the Mid-North Part of Great Xing'an Range. *J. Jilin Univ.* **2016**, *46*, 482–498. (In Chinese)
38. Defant, M.J.; Drummond, M.S. Derivation of some modern arc magmas by melting of young subducted lithosphere. *Nature* **1990**, *347*, 662–665. [CrossRef]
39. Hamelin, C.; Dosso, L.; Hanan, B.; Barrat, J.A. Sr-Nd-Hf isotopes along the Pacific Antarctic Ridge from 41 to 53° S. *Geophys. Res. Lett.* **2010**, *37*, 1–5. [CrossRef]
40. Tu, X.L.; Zhu, B.Q.; Fan, S.K.; Hu, A.Q. Pb isotopic composition of granulite facies belt in North China and its global comparison. *Sci. China* **1993**, *23*, 537–544. (In Chinese)
41. Yang, D.B.; Xu, W.L.; Pei, F.P.; Wang, Q.H.; Gao, S. Chronology and Pb isotope compositions of Early Cretaceous adakitic rocks in Xuzhou-Huaibei area, central China: Constraints on magma sources the eastern North China Craton. *Acta Tecton. Evol. Petrol. Sin. China* **2008**, *24*, 1745–1758. (In Chinese)
42. Li, S.G.; Yang, W. Decoupling of surface and subsurface sutures in the Dabie orogen and a continent-collisional lithospheric-wedging model: Sr-Nd-Pb isotopic evidences of Mesozoic igneous rocks in eastern China. *Chin. Sci. Bull.* **2003**, *48*, 831–838. [CrossRef]
43. Yang, D.B.; Xu, W.L.; Pei, F.P.; Yang, C.H.; Wang, Q.H. Spatial extent of the influence of the deeply subducted South China Block on the southeastern North China Block: Constraints from Sr-Nd-Pb isotopes in Mesozoic mafic igneous rocks. *Lithos* **2012**, *136*, 246–260. [CrossRef]

44. La Tourrette, T.; Hervig, R.L.; Holloway, J.R. Trace element partitioning between amphibole, phlogopite, and basanite melt. *Earth Planet. Sci. Lett.* **1995**, *135*, 13–30. [CrossRef]
45. Xu, W.L.; Wang, Q.H.; Wang, D.Y.; Pei, F.P.; Gao, S. Processes and mechanism of Mesozoic lithospheric thinning in eastern North China Craton: Evidence from Mesozoic igneous rocks and deep-seated xenoliths. *Earth Sci. Front.* **2004**, *11*, 309–317. (In Chinese)
46. Wang, K.; Burov, E.; Gumiaux, C.; Chen, Y.; Lu, G.; Mezri, L.; Zhao, L. Formation of Metamorphic Core Complexes in Non-Over-Thickened Continental Crust: A Case Study of Liaodong Peninsula (East Asia). *Lithos* **2015**, *238*, 86–100. [CrossRef]
47. Zhu, G.; Chen, Y.; Jiang, D.Z.; Lin, S.Z. Rapid change from compression to extension in the North China Craton during the Early Cretaceous: Evidence from the Yunmengshan metamorphic core complex. *Tectonophysics* **2015**, *656*, 91–110. [CrossRef]
48. Wang, Y.; Houseman, G.A.; Lin, G.; Guo, F.; Wang, Y.; Fan, W.; Chang, X. Mesozoic Lithospheric Deformation in the North China Block Numerical Simulation of Evolution from Orogenic Belt to Extensional Basin system. *Tectonophysics* **2005**, *405*, 47–63. [CrossRef]
49. Zheng, Y.F.; Xu, Z.; Zhao, Z.F.; Dai, L.Q. Mesozic mafic magmatism in North China: Implications for thinning and destruction of cratonic lithosphere. *Sci. China* **2018**, *48*, 379–414. (In Chinese)
50. Zhu, R.X.; Xu, Y.G.; Zhu, G.; Zhang, H.F.; Xia, Q.K.; Zheng, T.Y. Destruction of the North China Craton. *Sci. China* **2012**, *42*, 1135–1159. (In Chinese) [CrossRef]
51. Deng, J.; Yang, L.Q.; Groves, D.I.; Zhang, L.; Wang, Q.F. An integrated mineral system model for the gold deposits of the giant Jiaodong province, eastern China. *Earth-Sci. Rev.* **2020**, *208*, 103274. [CrossRef]
52. Qiu, K.F.; Goldfarb, R.J.; Deng, J.; Yu, H.C.; Gou, Z.Y.; Ding, Z.J.; Wang, Z.K.; Li, D.P. Gold deposits of the Jiaodong Peninsula, eastern China. *SEG Spec. Publ.* **2020**, *23*, 753–773.